Journal of Materials Chemistry C

ROYAL SOCIETY OF CHEMISTRY

PAPER

View Article Online
View Journal | View Issue

Cite this: J. Mater. Chem. C, 2021, 9, 10309

Strong sensitivity enhancement in lifetime-based luminescence thermometry by co-doping of $SrTiO_3:Mn^{4+}$ nanocrystals with trivalent lanthanide ions†

W. M. Piotrowski, [a] K. Trejgis,[a] M. Dramicanin [b] and L. Marciniak *[a]

Received 17th June 2021,
Accepted 13th July 2021

DOI: 10.1039/d1tc02814f

rsc.li/materials-c

The co-doping of $SrTiO_3:Mn^{4+}$ luminescent nanocrystals with trivalent lanthanide ions (Ln^{3+} = Lu^{3+}, Tm^{3+}, Er^{3+}, Ho^{3+}, Dy^{3+}, Eu^{3+}, and La^{3+}) is demonstrated as a new strategy for significant sensitivity improvement of lifetime-based luminescent thermometers. $SrTiO_3:Mn^{4+}:Ln^{3+}$ nanocrystals of about 25 nm diameter were prepared by the modified Pechini method and characterized using X-ray powder diffraction and electron microscopy techniques. The temperature dependence of Mn^{4+} emission in $SrTiO_3$ was considerably altered by the co-doping of Ln^{3+} due to the cooperating effects of $Mn^{4+} \rightarrow Ti^{3+}$ and $Mn^{4+} \rightarrow Ln^{3+}$ energy transfers. A substantial enhancement of the relative sensitivity of lifetime-based thermometry as high as 145% with respect to the unco-doped nanocrystals reveals the success of the approach. The obtained values of maximal relative sensitivity for different Ln^{3+} co-dopants are 5.10% K^{-1} at 290 K for Er^{3+}, 5.00% K^{-1} at 301 K for Eu^{3+}, 4.84% K^{-1} at 303 K for Dy^{3+}, 4.71% K^{-1} at 289 K for Ho^{3+}, and 3.87% K^{-1} at 290.7 K for Lu^{3+}.

Introduction

Luminescence thermometry (LT) enables the remote temperature measurements from changes in the luminescence properties of the phosphor.[1–8] These days, the general trend in LT aims to improve the reliability of the temperature readouts and simplify measurement methodology.[5,7] LT is mainly focused on two techniques for temperature readout from luminescence where the temperature is determined based on the (i) intensity ratio of two emission bands (the steady-state technique, the luminescence intensity ratio method – LIR) and (ii) the kinetics of the emission (the time-resolved technique, the lifetime method).[9–19] Both approaches provide self-referencing temperature readouts and present some advantages over one another. The LIR technique is faster to operate, simpler, and requires less sophisticated instrumentation than the lifetime method.[20–27] However, one of the major LIR shortcomings is related to the effect of spectral heterogeneity of the transmittance of the measuring medium which may lead to a change in the shape of the luminescence spectrum and thus an erroneous temperature readout.[28–30] This effect does not occur in luminescent thermometers based on the lifetime of the excited level.[5] Unfortunately, in this case, the commonly obtained thermometer sensitivities to temperature changes are much lower than in the case of the luminescence intensity ratio counterparts.[5,16–18,31,32] Therefore, extensive research is ongoing to develop new phosphors and/or to thermally activate different physical processes taking place in them to improve the sensitivity of lifetime-based luminescent thermometers. Recently, it has been shown that the $SrTiO_3:Mn^{4+}$ nanocrystals show favourable thermometric properties not only in the LIR approach but also in the lifetime-based approach.[33] The position of the Mn^{4+} emission in $SrTiO_3:Mn^{4+}$ at 725 nm results from the location of the ^2E emitting state of the Mn^{4+} ions at relatively low energy compared to other Mn^{4+} doped phosphors. This is related to both the relatively long Ti–O bond lengths (1.95 A) compared to other Mn^{4+} doped phosphors which slightly decrease in energy with decreasing crystal field strength according to the Tanabe–Sugano diagram and with the covalency and the corresponding nephelauxetic effect. According to the calculation performed by Brik *et al.* in order to enhance the relative sensitivity of LT based on the Mn^{4+} luminescence, the host material should have the lowest possible β_1 value and low energies of the $^4T_2$ and ^2E levels. Versatile analysis revealed that among all oxide and fluoride host materials reported so far, $SrTiO_3$ showed the lowest β_1 value of 0.9102, and the lowest energies of ^2E level of 13 795 cm^{-1} and $^4T_2$ level of 18 201 cm^{-1},[34] thus being the most promising host for Mn^{4+} for thermometric applications. The maximum relative sensitivity of this kind of luminescent thermometer has been

[a] Institute of Low Temperature and Structure Research, Polish Academy of Sciences, Okólna 2, 50-422 Wroclaw, Poland. E-mail: l.marciniak@intibs.pl
[b] Vinča Institute of Nuclear Sciences – National Institute of the Republic of Serbia, University of Belgrade, P.O. Box 522, Belgrade 11001, Serbia

† Electronic supplementary information (ESI) available. See DOI: 10.1039/d1tc02814f

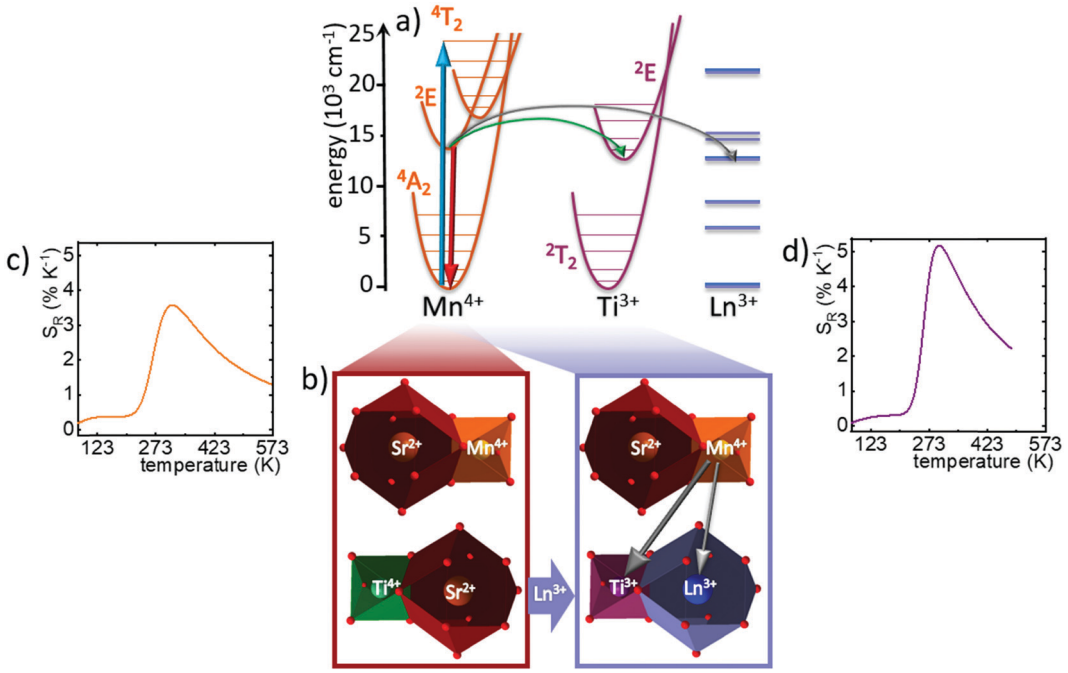

Fig. 1 The visualization of the concept of the proposed approach: simplified energy diagram of Mn^{4+}, Ti^{3+} and Ln^{3+} ions – (a); the polyhedral visualization of the substitution of the octahedral Ti^{4+} sites with Mn^{4+} ions and cuboctahedrally coordinated Sr^{2+} sites with Ln^{3+} ions in the $SrTiO_3$:Mn^{4+} structure – (b); thermal evolution of relative sensitivity $S_R(\tau_{avr})$ of $SrTiO_3$:Mn^{4+} – (c) and $SrTiO_3$:Mn^{4+},Tm^{3+} – (d) nanocrystals.

reported as S_R = 3.57% K^{-1} at 318 K. Our recent findings indicate that the co-doping of the $SrTiO_3$ nanocrystals with lanthanide (Ln^{3+}) ions leads to the reduction of the Ti^{4+} to the Ti^{3+} ions.[35] Since Ti^{3+} is optically active and the position of its energy levels is located in the close vicinity of the ^2E state of Mn^{4+}, co-doping with Ln^{3+} is presented in this paper as a novel strategy for the improvement of the relative sensitivity of the lifetime-based $SrTiO_3$:Mn^{4+},Ln^{3+} luminescent thermometer. The main conception of the manuscript is presented in Fig. 1. According to the previously reported results[35] the introduction of Ln^{3+} ions to the Sr^{2+} sites in the $SrTiO_3$ structure induces charge compensation by the local reduction of titanium from Ti^{4+} to Ti^{3+}. Therefore, the doping of the $SrTiO_3$ lattice with Mn^{4+} and any of Ln^{3+} ions shall contain also the optically active Ti^{3+} centers. Moreover, the excited state of Ti^{3+} ions is energetically located slightly below the ^2E level of Mn^{4+} ions (around 1100 cm^{-1}) and thus extremely efficient energy transfer $Mn^{4+} \rightarrow Ti^{3+}$ should be expected. Additionally, the 4f states of the Ln^{3+} ions may lead to the $Mn^{4+} \rightarrow Ln^{3+}$ energy transfer which may further enhance the sensitivity of luminescent thermometer.

Experimental

$SrTiO_3$:0.1%Mn^{4+} and $SrTiO_3$:0.1%Mn^{4+}, 1%Ln^{3+} (Ln^{3+} = Lu^{3+}, Tm^{3+}, Er^{3+}, Ho^{3+}, Dy^{3+}, Eu^{3+}, La^{3+}) nanopowders were synthesized using the modified Pechini method.[36] Strontium nitrate ($Sr(NO_3)_2$ of 99.9965% purity from Alfa Aesar), titanium(IV) *n*-butoxide ($Ti(OC_4H_9)_4$ with 99+% purity from Alfa Aesar), 2,4-pentanedione ($C_5H_8O_2$ with 99% purity from Alfa Aesar), citric acid ($C_6H_8O_7$ of 99% purity from Sigma Aldrich) and different lanthanide oxides: lutetium oxide (Lu_2O_3 with 99.995% purity from Stanford Materials Corporation), thulium oxide (Tm_2O_3 of 99.99% purity from Alfa Aesar), erbium oxide (Er_2O_3 of 99.999% purity from Sigma Aldrich), holmium oxide (Ho_2O_3 of 99.997% purity from Stanford Materials Corporation), dysprosium oxide (Dy_2O_3 of 99.999% purity from Stanford Materials Corporation), europium oxide (Eu_2O_3 of 99.99% purity from Stanford Materials Corporation) and lanthanum oxide (La_2O_3 of 99.99% purity from Stanford Materials Corporation) were used as the starting compounds. An appropriate amount of nitrates was dissolved in deionized water. In the case of Ln^{3+} co-doped nanocrystals, to obtain nitrates from oxides, their stoichiometric amounts were diluted in an aqueous solution of ultrapure nitric acid. Then, all aqueous solutions of nitrates were mixed together. Subsequently, an appropriate amount of $Ti(OC_4H_9)_4$ was measured out into a small laboratory beaker; then, a solution of 2,4-pentanedione in a stoichiometric ratio of 1 : 1 was added to stabilize $Ti(OC_4H_9)_4$ solution. The contents of the beaker were gently stirred to obtain a transparent, yellowish solution, which then was combined with the nitrate solution. After this, the solution was mixed with anhydrous citric acid. Subsequently, the obtained solution was dried for 1 week at 363.15 K until a resin was formed and annealed at 1173.15 K for 3 hours in air atmosphere.

All materials were examined by X-ray powder diffraction (XRPD) measurements carried out using a PANalytical X'Pert diffractometer, equipped with an Anton Paar TCU 1000 N temperature control unit, using Ni-filtered Cu-K_α radiation (V = 40 kV, I = 30 mA).

Transmission electron microscope (TEM) images were taken using a Philips CM-20 SuperTwin TEM microscope. The samples

were dispersed in methanol, and a droplet of this suspension was put on a microscope copper grid. Next, the samples were dried and purified in a plasma cleaner. Studies were performed using a conventional TEM procedure with 160 kV parallel beam electron energy.

The emission spectra were measured using the 400 nm excitation lines from a laser diode and a Silver-Nova Super Range TEC spectrometer from Stellarnet (1 nm spectral resolution) as the detector. The temperature of the sample was controlled using a THMS 600 heating–cooling stage from Linkam (0.1 K temperature stability and 0.1 K set point resolution).

The excitation spectra and luminescence decay profiles were recorded using a FLS1000 Fluorescence spectrometer from Edinburgh Instruments with a 450 W xenon lamp and μFlash lamp as the excitation sources and a R928P side window photomultiplier tube from Hamamatsu as the detector. The average lifetimes of the excited states were calculated with the use of double exponential function using eqn (S1), ESI.†

Results and discussion

Structural and morphological characterization

$SrTiO_3$ is one of the most widely investigated compounds from the family of perovskite oxides with a general chemical formula of ABO_3.[37–42] In the case of strontium titanate, the 'B' sites occupied by Ti^{4+} ions are octahedrally coordinated to six O^{2-} anions while the Sr^{2+} cations are cuboctahedrally coordinated to the 'A' sites between the Ti^{4+} octahedrons. Since manganese ions may exist in both the Mn^{2+} and Mn^{4+} oxidation states; theoretically, manganese ions may occupy both the Sr^{2+} and Ti^{4+} sites. In this case, the occupation of the octahedral Ti^{4+} sites with Mn^{4+} (effective ionic radii (EIR) = 53 pm) is clear and may be highly probable: $EIR_{Mn^{4+}}/EIR_{Ti^{4+}}$ = 53 pm/60.5 pm ≈ 0.87. Therefore, due to the difference in the effective ionic radii and in the coordination number mainly the Mn^{4+} ions in the Ti^{4+} position are observed in the $SrTiO_3$ structure.[33,43–46] Additionally Mn^{4+} as a $3d^3$ ion is thermodynamically extremely stabilized in the octahedral fields. On the other hand, the presence of Mn^{2+} in the Sr^{2+} sites in $SrTiO_3$ was reported by *e.g.* Tkach *et al.* in ceramics[47] and Yang *et al.* in the nanocrystals[48] when these materials were synthesized under favourable conditions, *i.e.* with the stoichiometric deficit of Sr^{2+} ions. There are no ionic radii reported by Shannon for the Mn^{2+} ions with coordination number (CN) above 8 (EIR = 96 pm for 8-fold coordinated Mn^{2+} ions).[43] However, Trepokov *et al.*[49] and Tkach *et al.*[47] suggest the extrapolation to CN = 12 from the EIR values of Mn^{2+} for lower CN with the EIR = 127 pm as a result. In this case, the misfit factor would equal $EIR^{XII}_{Mn^{2+}}/EIR^{XII}_{Sr^{2+}}$ = 127 pm/144 pm ≈ 0.88 instead of $EIR^{VIII}_{Mn^{2+}}/EIR^{XII}_{Sr^{2+}}$ = 96 pm/144 pm ≈ 0.67. However, the EIR *vs.* CN dependence is not clearly described and Shannon[43] intentionally did not present the ionic radius for Mn^{2+} with CN = 12. Nevertheless, the results from the mentioned papers lead to the conclusion that both Mn^{2+} and Mn^{4+} ions may be successfully located in the $SrTiO_3$ lattice depending on the deficit of Sr^{2+} or Ti^{4+}, respectively, and for the synthesis of $SrTi_{1-x}Mn_xO_3$ compound, the only Mn^{4+} substituting Ti^{4+} ions should be expected. To validate the phase purity of the synthesized phosphors, the X-ray powder diffraction (XRPD) patterns were analysed (Fig. 2a). Regardless of the dopant, the $SrTiO_3$ structure was obtained with no additional phases. In the case of the sample doped with 0.1% Mn^{4+}, the observed shift of peak positions by ~0.03° toward higher angles in comparison to the reference pattern (ICSD 187296) is a consequence of the contraction of the unit cell corresponding to the Ti^{4+} with smaller Mn^{4+} ions (Fig. S1, ESI†). This result clearly confirms that the Ti^{4+} site cannot be substituted by Mn^{3+} or Mn^{2+} ions which would extend the cell size (EIR = 64.5 and 83 pm for high spin with CN = 6, respectively). On the other hand, the XRPD patterns of $SrTiO_3$ doped with Mn^{4+} and different Ln^{3+} ions (Table S1, ESI†) are shifted toward lower angles. The Ln^{3+} preferably occupy the Sr^{2+} sites and all of them are characterized by lower EIR than Sr^{2+} which should cause even deeper contraction. However, as shown recently, due to the difference in the ionic charge, the introduction of the Ln^{3+} ions in the Sr^{2+} site of the $SrTiO_3$:Ln^{3+} structure leads to

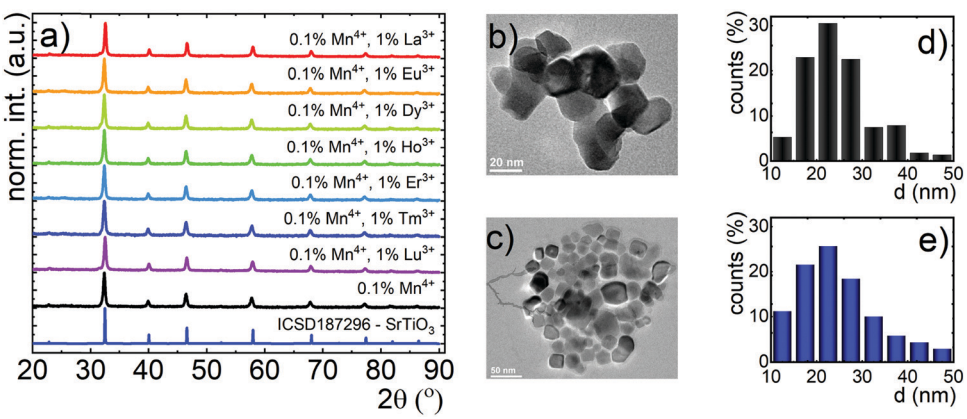

Fig. 2 Structural characterization of the synthesized materials: the X-ray diffraction patterns of $SrTiO_3$:Mn^{4+} with different Ln^{3+} dopants – (a); the representative TEM images of $SrTiO_3$:Mn^{4+} – (b) and $SrTiO_3$:Mn^{4+},Tm^{3+} powders – (c); and the particle size distributions for $SrTiO_3$:Mn^{4+} powder – (d) and $SrTiO_3$:Mn^{4+},Tm^{3+} nanocrystals – (e).

the reduction of Ti^{4+} to Ti^{3+}. In this case, the Ti^{3+} with EIR = 67 pm in the octahedral coordination (CN = 6), which has a greater impact on the local symmetry in comparison to the dodecahedral Sr^{2+}/Ln^{3+} site, generates the enlargement of the cell size which is in the agreement with the presented results. Additionally, the analysis of the transmission electron microscopy (TEM) images is presented for the representative powders of $SrTiO_3$ doped with Mn^{4+} and co-doped with Mn^{4+} and Tm^{3+} (Fig. 2b and c). The analysis indicated that the nanocrystals formed well-crystalized and mostly agglomerated particles. For both phosphors, the average grain size achieved similar magnitudes, namely average Feret diameters were D_f = 27.0 nm and 24.6 nm for $SrTiO_3$:Mn^{4+} and $SrTiO_3$:Mn^{4+},Tm^3, respectively (Fig. 2d and e).

In the case of the $SrTiO_3$:Mn^{4+} nanocrystals, the mechanism responsible for the luminescence of Mn^{4+} ions is depicted in Fig. 3a. The λ_{exc} = 400 nm laser diode (25 000 cm^{-1}, blue arrow in Fig. 3a) excites electrons from the ground $^4A_2$ state of Mn^{4+} to its $^4T_1$ state. After this, because of the nonradiative processes, the ^2E state is populated and its radiative depopulation leads to the occurrence of the emission band centered at 725 nm ($^2E \rightarrow {}^4A_2$ electronic transition). At elevated temperatures, the Mn^{4+} emission starts quenching since the higher vibrational state of the ^2E parabola starts to be gradually occupied, and, when the provided thermal energy exceeds the energy at which the ^2E and $^4T_2$ parabola intersects each other, the nonradiative processes becomes more pronounced. However, when the Ln^{3+} ions are introduced to the structure as the co-dopant, two additional processes are activated. First of them is the $Mn^{4+} \rightarrow Ln^{3+}$ energy transfer, which due to the energy mismatch of the ^2E state and the 4f states of the Ln^{3+} should occur with the assistance of the phonon. Therefore, the presence of these additional nonradiatively depopulating channels of the ^2E state will lead to both shortening of the lifetime of the ^2E state and its thermal quenching rate. However, as shown recently,[35] the difference in the ionic charge between the dopant and the Sr^{2+} ions leads to the reduction of Ti^{4+} to Ti^{3+}, which is an optically active ion. Therefore, the Ti^{3+} ^2E excited state which is localized below the ^2E state of Mn^{4+} becomes the acceptor in the $Mn^{4+} \rightarrow Ti^{3+}$ energy transfer. This effect was confirmed by the observation of the change in the emission thermal quenching rate of the nanocrystals co-doped with optically inactive ions $SrTiO_3$:Mn^{4+},La^{3+} and $SrTiO_3$:Mn^{4+},Lu^{3+}. The co-dopant does not affect the spectral position of the $^2E \rightarrow {}^4A_2$ emission bands which means that any significant changes in the crystal field strength after Ln^{3+} co-doping are not observed (Fig. 3b). Except the Tm^{3+}, the emission band of the Ln^{3+} ions cannot be observed in the spectral range which overlaps with

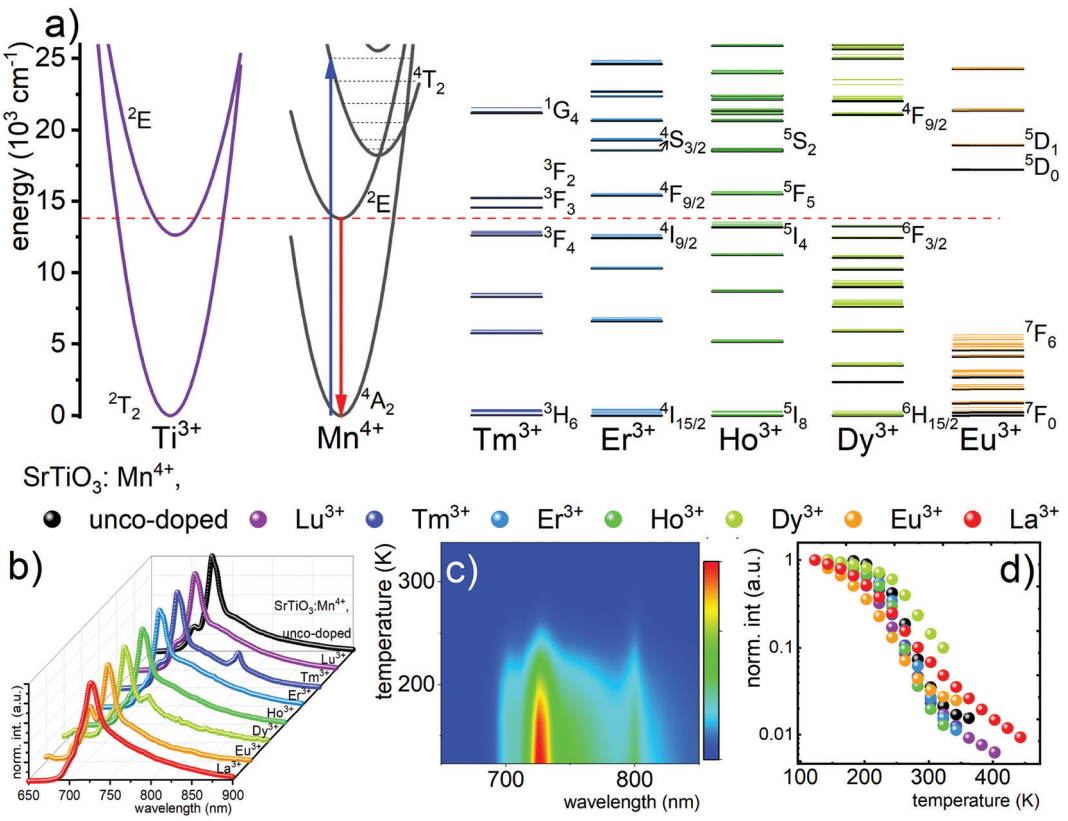

Fig. 3 Configurational coordinate diagrams for Ti^{3+}, Mn^{4+} and different Ln^{3+} ions (Tm^{3+}, Er^{3+}, Ho^{3+}, Dy^{3+}, and Eu^{3+}) – (a); the emission spectra of Mn^{4+} ions measured at 123 K for $SrTiO_3$ powders doped with Mn^{4+} and different Ln^{3+} ions – (b); the emission map as a function of temperature for representative $SrTiO_3$:Mn^{4+},Tm^{3+} sample – (c); and thermal evolution of the integral band intensities of the $^2E \rightarrow {}^4A_2$ transition of Mn^{4+} ion for different Ln^{3+} ions in $SrTiO_3$:Mn^{4+},Ln^{3+} nanocrystals – (d).

the $^2E \rightarrow {}^4A_2$ band of Mn^{4+} ions. To analyze the possible $Mn^{4+} \rightarrow Ln^{3+}$ energy transfer, the position of the 4f energy levels localized in the closest energetical vicinity of the ^2E state of Mn^{4+} should be considered (Table 1). In this study, the exact energy of the ^2E energy level used for the calculation was based on the Brik's and Avram's calculations.[50] The small energy difference between the ^2E and 4f states of Ln^{3+} facilitates the interionic energy transfer. From this perspective, it can be clearly seen that the most beneficial energy level configuration has Tm^{3+} with both the $^3F_3$ and $^3F_4$ levels located with the energetic distance below 1000 cm^{-1} from the Mn^{4+} emitting state. The $^5I_4$ level of Ho^{3+} ions is the closest to the ^2E level ($\sim$300 cm^{-1}) in contrast to its upper level $^5F_5$ (above 1600 cm^{-1}). A similar situation is observed for Dy^{3+}; however, both states are in the slightly larger energy distance from the ^2E of Mn^{4+}. The largest energy separation was observed for Eu^{3+} ions where the $^5D_0$ state is localized 3460 cm^{-1} above the ^2E state.

Independent of the use of Ln^{3+} co-dopant, the excitation spectra for Mn^{4+} emission (λ_{em} = 725 nm) consist of two broad bands related to the $^4A_2 \rightarrow {}^4T_1$ (with the maximum at 400 nm) and $^4A_2 \rightarrow {}^4T_2$ (centered at around 530 nm) transitions (Fig. S2, ESI†). Therefore, the use of a 400 nm laser diode as the pumping source provides the efficient excitation of Mn^{4+} ions and its emission at $\sim$725 nm corresponding to the $^2E \rightarrow {}^4A_2$ transition (Fig. 3b and Fig. S3, ESI†). $SrTiO_3$ is found to be a host material of one of the lowest crystal field strength among all Mn^{4+} doped phosphors (D_q/B = 2.47).[50] Moreover, the relatively low value of the activation energy between the ^2E and $^4T_2$ states found for the $SrTiO_3$:Mn^{4+} nanocrystals ($\Delta E_a \approx$ 2950 cm^{-1}) makes this phosphor especially attractive from the luminescence thermometry perspective.[33] Therefore, to evaluate the luminescence thermal quenching in the $SrTiO_3$:Mn^{4+},Ln^{3+} nanocrystals, their emission intensity ratio was analyzed in a wide temperature range (Fig. 3c, and Fig. S4, ESI†). To avoid the spectral overlapping of the Mn^{4+} and Ln^{3+} emission bands which may affect the accuracy of the performed readout (which is especially problematic for the $^4F_{9/2} \rightarrow {}^6H_{9/2}$ transition of Dy^{3+} at $\sim$751 nm or $^5D_0 \rightarrow {}^7F_4$ of Eu^{3+} at $\sim$700 nm), the Mn^{4+} emission signal was integrated in the 720–740 nm spectral range (Fig. 3d). The Mn^{4+} emission intensity for $SrTiO_3$:Mn^{4+} nanocrystals remains unchanged up to around 203 K above which drastic quenching of intensity by almost two orders of magnitude can be observed. However, the thermal dependence of Mn^{4+} emission intensity changes when the nanocrystals are co-doped with the Ln^{3+} ions. In the case of the La^{3+} and Lu^{3+} co-doped systems, the quenching process starts around 143 K due to the $Mn^{4+} \rightarrow Ti^{3+}$ energy transfer. The Mn^{4+} emission intensity of the $SrTiO_3$:Mn^{4+},La^{3+} nanocrystals decreases with a smaller and almost constant slope in the analyzed temperature range when compared to the intensity of the Lu^{3+} co-doped counterpart. On the other hand, in the case of the Lu^{3+} doped nanocrystals, an increase in the luminescence thermal quenching rate above 180 K can be observed. Due to the lack of the 4f energy state and the similarities in the electronic charge, the observed differences in the Mn^{4+} thermal quenching rates can be explained in terms of the differences in the ionic radii of the co-dopants. The difference in the size of the ions localized in the second coordination sphere of the Ti^{3+} ions may modify its crystal field strength and thus change the position of the ^2E state of Ti^{3+}. As a consequence, the probability of thermally dependent $Mn^{4+} \rightarrow Ti^{3+}$ energy transfer will be modified. The analysis starts to be more complex when the optically active Ln^{3+} ions are introduced to the $SrTiO_3$ structure due to the additional $Mn^{4+} \rightarrow Ln^{3+}$ energy transfer routes. The fastest thermal quenching of the $^2E \rightarrow {}^4A_2$ emission intensity was observed for $SrTiO_3$:Mn^{4+},Tm^{3+} while the slowest was observed in the case of $SrTiO_3$:Mn^{4+},Dy^{3+} nanocrystals.

An increase in the luminescence thermal quenching rate associated with Ln^{3+} co-doping may suggest the beneficial influence of the co-doping process on the thermometric properties of lifetime based luminescent thermometers in $SrTiO_3$:Mn^{4+},Ln^{3+} nanocrystals. Indeed, an increase in temperature results in the shortening of the luminescence decay profile of the ^2E state of Mn^{4+} ions and the gradual deviation from their exponential shape (Fig. 4a and Fig. S5, ESI†). Therefore, to perform a comparative analysis on the influence of temperature on the decay kinetics, the average lifetimes were (τ_{avr}) calculated according to the procedure described in the ESI† (eqn (S1) and (S2)). The initial analysis indicates that at low temperature (at 123 K) τ_{avr} undergoes the shortening from the τ_{avr} = 1.72 ms for $SrTiO_3$:Mn^{4+} to 0.53 ms for $SrTiO_3$:Mn^{4+},Tm^{3+} nanocrystals. Above 200 K, the thermal shortening of the τ_{avr} can be observed for all the nanocrystals, however, with different thermal quenching rates. The thermal dependence of the τ_{avr} of Mn^{4+} can be very well fitted by the theoretical dependence (eqn (1) and Fig. 4b):

$$\tau(T) = \frac{\tau_R(0) \cdot \tanh(h\nu/2k_BT)}{1 + (\tau_R(0) \cdot \tanh(h\nu/2k_BT)/\tau_{NR}) \cdot \exp(-\Delta E/k_BT)}, \quad (1)$$

where $\tau_R(0)$ is the radiative lifetime at T = 0 K, k_B = 0.69503476 cm^{-1} K^{-1} is the Boltzmann constant, $h\nu$ is the average energy of phonons coupled to the $^2E \rightarrow {}^4A_2$ transition, $1/\tau_{NR}$ is the non-radiative decay rate, and ΔE is the activation energy of the process. To quantify the observed thermally-induced variation of τ_{avr}, the absolute (S_A) relative sensitivity (S_R) of luminescent thermometers was calculated using the following equations:

$$S_A = \frac{\Delta\tau_{avr}}{\Delta T}, \quad (2)$$

Table 1 The differences between the ^2E level of Mn^{4+} and Ln^{3+} states located above and below it

Co-dopant ion	Tm^{3+}	Er^{3+}	Ho^{3+}	Dy^{3+}	Eu^{3+}
Excited state above ^2E	$^3F_3$	$^4F_{9/2}$	$^5F_5$	$^4F_{9/2}$	$^5D_0$
Energy (cm^{-1})	689	1591	1658	7228	3436
Excited state below ^2E	$^3F_4$	$^4I_{9/2}$	$^5I_4$	$^6F_{3/2}$	$^7F_6$
Energy (cm^{-1})	940	1107	299	560	8144

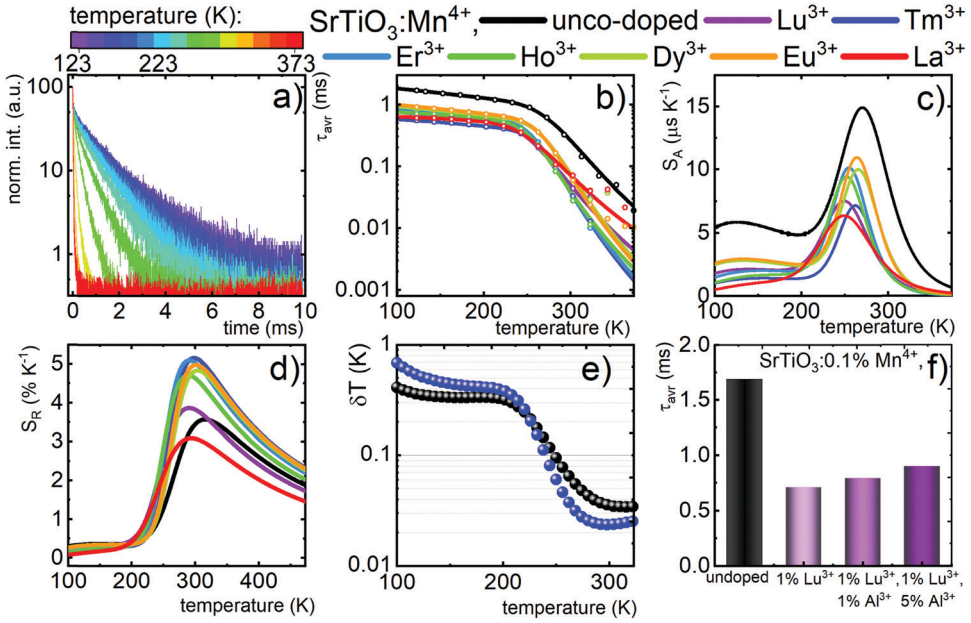

Fig. 4 Thermal evolution of luminescence decays of the ^2E excited state of Mn^{4+} for the representative $SrTiO_3$:Mn^{4+},Eu^{3+} nanocrystals – (a); thermal evolution of average lifetime τ_{avr} of the ^2E excited state of Mn^{4+} ions – (b), absolute sensitivities S_A – (c) and relative sensitivities S_R – (d) of $SrTiO_3$:Mn^{4+},Ln^{3+}; thermal dependence of temperature estimation uncertainty for $SrTiO_3$:Mn^{4+} and $SrTiO_3$:Mn^{4+},Tm^{3+} (e); and the influence of charge compensator concentration (Al^{3+}) on τ_{avr} at 123 K for $SrTiO_3$:Mn^{4+},Lu^{3+},Al^{3+} – (f).

$$S_R = \frac{1}{\tau_{avr}} \cdot \frac{\Delta\tau_{avr}}{\Delta T} \times 100\%, \quad (3)$$

where $\Delta\tau_{avr}$ is the change in the lifetime of the ^2E excited state corresponding to the change of temperature ΔT. The highest values of S_A were found for $SrTiO_3$:Mn^{4+} nanocrystals with the maximum at S_{Amax} = 14.93 μs K^{-1} at 273 K (Fig. 4c). The smaller values of S_A observed for Ln^{3+} co-doped nanocrystals result from the shorter τ_{avr} values in those cases. However, when S_R is considered the favorable influence of the Ln^{3+} ions on the thermometric properties of these nanocrystals can be clearly confirmed (Fig. 4d). The maximal value of S_R = 3.57% K^{-1} at 318 K was found. The introduction of Ln^{3+} ions increases the S_R up to 5.19% K^{-1} for $SrTiO_3$:Mn^{4+},Tm^{3+} at 298 K. This significant enhancement of the relative sensitivity by around 145% with respect to the unco-doped nanocrystals reveals the beneficial role of the Ln^{3+} ions. The maximum values of relative sensitivity in the case of the nanocrystals with other co-dopant were as follows: 5.10% K^{-1} at 290 K for Er^{3+} ions, 5.00% K^{-1} at 301 K for Eu^{3+} ions, 4.84% K^{-1} at 303 K for Dy^{3+} ions 4.71% K^{-1} at 289 K for Ho^{3+} ions, and 3.87% K^{-1} at 290.7 K for Lu^{3+}. Only in the case of the La^{3+} co-doped nanocrystal a lower S_R with respect to that of the un-co-doped counterparts was observed which results from the lower slope of the $\tau_{avr}(T)$ dependence. As discussed above, the quenching of the Mn^{4+} emission intensity starts at lower temperatures in this case which results in the continuous quenching of the $^2E \rightarrow {}^4A_2$ luminescence in the considered temperature range. This causes the broadening of the usable temperature range of this luminescent thermometer since the $S_R > 1\%$ K^{-1} can be observed already above 325 K for $SrTiO_3$:Mn^{4+},La^{3+}. It is noteworthy that it the case of thermal imaging using the lifetime approach usually two intensity frames are divided by each other to receive a 2D thermal map. Therefore, the acquisition time in this case is limited by the value of τ_{avr}. Therefore, although the shortening of τ_{avr} observed after the introduction of the Ln^{3+} co-dopants is beneficial from the relative sensitivity perspective it may affect the quality of thermal imaging by the limitation of the maximal available acquisition time. Nevertheless, for thermal imaging of the fast processes, the short τ_{avr} is favorable. Additional parameter which enables the verification of the quality of temperature readout using the luminescent thermometer is the temperature determination uncertainty calculated as follows:

$$\delta T = \frac{1}{S_R} \frac{\delta\tau_{avr}}{\tau_{avr}} \quad (4)$$

where $\delta\tau_{avr}/\tau_{avr}$ is the uncertainty in the determination of τ_{avr} (determined as a standard deviation in 30 measurements of τ_{avr}) (Fig. S6, ESI†). Due to the introduction of the Ln^{3+} co-dopants the temperature determination uncertainty decreases from δT = 0.034 K at 310 K for $SrTiO_3$:Mn^{4+} to δT = 0.020 K for $SrTiO_3$:Mn^{4+},Tm^{3+} nanocrystals (Fig. 4e). Even the presence of Lu^{3+} ions enables the reduction of δT with respect to the unco-doped counterpart. In order to confirm that the reduction of the titanium ions to the Ti^{3+} oxidation state is responsible for the changes in the spectroscopic properties of the $SrTiO_3$:Mn^{4+},Lu^{3+} nanocrystals, the charge compensation has been used by the introduction of ions which (i) prefer the (3+) oxidation state, (ii) are optically inactive and (iii) may substitute the octahedral site of the Ti^{4+}. All these requirements are met by the Al^{3+} ions (Fig. S7, ESI†). The charge compensation can be written as follows:

$$SrTiO_3 \rightarrow Ti(4+) \rightarrow Sr(2+) \rightarrow Ti(4+) \rightarrow (10+) \quad (5)$$

$$SrTiO_3{:}Mn^{4+} \rightarrow Mn(4+) \rightarrow Sr(2+) \rightarrow Ti(4+) \rightarrow (10+) \quad (6)$$

$$SrTiO_3{:}Mn^{4+},Ln^{3+} \rightarrow Mn(4+) \rightarrow Ln(3+) \rightarrow Ti(3+) \rightarrow (10+) \quad (7)$$

$$SrTiO_3{:}Mn^{4+},Ln^{3+},Al^{3+} \rightarrow Mn(4+) \rightarrow Ln(3+) \rightarrow Al(3+) \rightarrow (10+) \quad (8)$$

The presence of the Al^{3+} ions lessens the probability of the $Ti^{4+} \rightarrow Ti^{3+}$ reduction and, thus, should reduce the quenching rate of the ^2E state of the Mn^{4+} ions. Since this process is possible when the Al^{3+} and Ln^{3+} ions are in the close vicinity, excess of Al^{3+} with respect to the Lu^{3+} should be used. As shown in Fig. 4f, the τ_{avr} of ^2E which has been shortened after Lu^{3+} introduction starts to gradually elongate when the concentration of Al^{3+} ions increases from 0.7 ms to 0.9 ms for 5% Al^{3+} ions (Fig. S8, ESI†). However, the further increase in the Al^{3+} amount leads to structural decomposition and the occurrence of additional reflections in the XRD patterns. The obtained results confirm that quenching of the ^2E state in the Lu^{3+} co-doped nanocrystals is caused by energy transfer to the Ti^{3+} ions. Although presented in this manuscript experimental results may confirm the hypothesis that the presence of the Ti^{3+} ions in the $SrTiO_3{:}Mn^{4+},Ln^{3+}$ nanocrystals are responsible for the enhancement of the relative sensitivity of the luminescent thermometer based on the lifetime of the ^2E state of the Mn^{4+} ions, further, more specific experiments such as concentration-dependent photoluminescence studies or magnetic measurements will follow to elaborate on the hypothesis of Ti^{3+} in future and enable to verify if other processes or nonintentional dopants could also be responsible for the discussed effect. Presented data confirm the highly favorable influence of Ln^{3+} co-doping on the thermometric properties of the lifetime based luminescent thermometers in $SrTiO_3{:}Mn^{4+},Ln^{3+}$ nanocrystals.

Conclusions

In this work, a strategy for the improvement of a lifetime-based luminescent thermometer in $SrTiO_3{:}Mn^{4+}$ nanocrystals by the introduction of Ln^{3+} ions is proposed and investigated in detail. It was found that the introduction of the Ln^{3+} ions leads to the quenching of the lifetime of the ^2E state and increases the thermal quenching rate. This effect was discussed in terms of the cooperation of two effects, $Mn^{4+} \rightarrow Ti^{3+}$ energy transfer and $Mn^{4+} \rightarrow Ln^{3+}$ energy transfer. In the case of the former, it was proved that the difference in the ionic charge between Sr^{2+} and the co-dopant Ln^{3+} ions leads to the reduction of Ti^{4+} to Ti^{3+} which efficiently quenches the Mn^{4+} luminescence. This effect can be compromised to some extent by the introduction of Al^{3+} ions as charge compensators. When the optically active Ln^{3+} ions are introduced to the nanocrystals, the cooperation of both the effects occurs leading to the enhancement of the relative sensitivity of the lifetime based luminescent thermometer by as much as 145% for $SrTiO_3{:}Mn^{4+},Tm^{3+}$ (S_R = 5.19%/K at 298 K) with respect to its unco-doped counterpart $SrTiO_3{:}Mn^{4+}$ (S_R = 3.57% K^{-1} at 318 K). Additionally, the presence of Ln^{3+} decreases the temperature determination uncertainty to δT = 0.020 K for $SrTiO_3{:}Mn^{4+},Tm^{3+}$ nanocrystals. These results clearly indicate that the proposed strategy enables the improvement of the thermometric properties of the lifetime based luminescent thermometry in strontium titanites and allows the development of highly sensitive lifetime based luminescent thermometers operating in biologically relevant temperatures.

Conflicts of interest

There are no conflicts to declare.

Acknowledgements

The ''High sensitive thermal imaging for biomedical and microelectronic application'' project was carried out within the First Team programme of the Foundation for Polish Science cofinanced by the European Union under the European Regional Development Fund.

References

1 X. D. Wang, O. S. Wolfbeis and R. J. Meier, *Chem. Soc. Rev.*, 2013, **42**, 7834–7869.
2 D. Jaque and F. Vetrone, *Nanoscale*, 2012, **4**, 4301–4326.
3 C. D. S. Brites, P. P. Lima, N. J. O. Silva, A. Millán, V. S. Amaral, F. Palacio and L. D. Carlos, *Thermometry at the nanoscale*, The Royal Society of Chemistry, 2012, vol. 4.
4 C. D. S. Brites, S. Balabhadra and L. D. Carlos, *Adv. Opt. Mater.*, 2019, **7**, 1801239.
5 A. Bednarkiewicz, L. Marciniak, L. D. Carlos and D. Jaque, *Nanoscale*, 2020, **12**, 14405–14421.
6 M. Dramićanin, in *Luminescence Thermometry*, ed. M. B. T.-L. T. Dramićanin, Woodhead Publishing, 2018, pp. 251–263.
7 M. D. Dramićanin, *J. Appl. Phys.*, 2020, **128**, 40902.
8 M. Suta and A. Meijerink, *Adv. Theory Simul.*, 2020, **3**, 2000176.
9 A. M. Kaczmarek, M. Suta, H. Rijckaert, T. P. van Swieten, I. Van Driessche, M. K. Kaczmarek and A. Meijerink, *J. Mater. Chem. C*, 2021, **9**, 3589–3600.
10 M. Runowski, P. Woźny and I. R. Martín, *J. Mater. Chem. C*, 2021, **9**, 4643–4651.
11 P. Bolek, J. Zeler, C. D. S. Brites, J. Trojan-Piegza, L. D. Carlos and E. Zych, *Chem. Eng. J.*, 2021, **421**, 129764.
12 M. Runowski, P. Wozny, N. Stopikowska, I. R. Martín, V. Lavín and S. Lis, *ACS Appl. Mater. Interfaces*, 2020, **12**, 43933–43941.
13 M. Runowski, A. Shyichuk, A. Tymiński, T. Grzyb, V. Lavín and S. Lis, *ACS Appl. Mater. Interfaces*, 2018, **10**, 17269–17279.
14 Y. Gao, Y. Cheng, T. Hu, Z. Ji, H. Lin, J. Xu and Y. Wang, *J. Mater. Chem. C*, 2018, **6**, 11178–11183.

15 L. Marciniak, A. Bednarkiewicz, D. Kowalska and W. Strek, *J. Mater. Chem. C*, 2016, **4**, 5559–5563.
16 L. Marciniak and K. Trejgis, *J. Mater. Chem. C*, 2018, **6**, 7092–7100.
17 M. Wu, D. Deng, F. Ruan, B. Chen and S. Xu, *Chem. Eng. J.*, 2020, **396**, 125178.
18 L. Marciniak, K. Elzbieciak-Piecka, K. Kniec and A. Bednarkiewicz, *Chem. Eng. J.*, 2020, **388**, 124347.
19 X. Chen, S. Liu, K. Huang, J. Nie, R. Kang, X. Tian, S. Zhang, Y. Li and J. Qiu, *Chem. Eng. J.*, 2020, **396**, 125201.
20 F. Vetrone, R. Naccache, A. Zamarrón, A. J. De La Fuente, F. Sanz-Rodríguez, L. M. Maestro, E. M. Rodriguez, D. Jaque, J. G. Sole and J. A. Capobianco, *ACS Nano*, 2010, **4**, 3254–3258.
21 C. D. S. Brites, S. Balabhadra and L. D. Carlos, *Adv. Opt. Mater.*, 2019, **7**, 1801239.
22 Y. Cheng, Y. Gao, H. Lin, F. Huang and Y. Wang, *J. Mater. Chem. C*, 2018, **6**, 7462–7478.
23 E. Casagrande, M. Back, D. Cristofori, J. Ueda, S. Tanabe, S. Palazzolo, F. Rizzolio, V. Canzonieri, E. Trave and P. Riello, *J. Mater. Chem. C*, 2020, **8**, 7828–7836.
24 J. Trojan-Piegza, C. D. S. Brites, J. F. C. B. Ramalho, Z. Wang, G. Zhou, S. Wang, L. D. Carlos and E. Zych, *J. Mater. Chem. C*, 2020, **8**, 7005–7011.
25 M. Łukaszewicz, R. Tomala and R. Lisiecki, *J. Mater. Chem. C*, 2020, **8**, 1072–1082.
26 G. H. Pan, L. L. Zhang, H. H. Wu, X. Qu, H. H. Wu, Z. Hao, L. L. Zhang, X. Zhang and J. Zhang, *J. Mater. Chem. C*, 2020, **8**, 4518–4533.
27 H. Suo, X. Zhao, Z. Zhang and C. Guo, *Chem. Eng. J.*, 2020, **389**, 124506.
28 K. T. V. Grattan, Z. Y. Zhang, T. Sun, Y. Shen, L. Tong and Z. Ding, *Meas. Sci. Technol.*, 2001, **12**, 981–986.
29 L. Labrador-Páez, M. Pedroni, A. Speghini, J. García-Solé, P. Haro-González and D. Jaque, *Nanoscale*, 2018, **10**, 22319–22328.
30 Y. Shen, J. Lifante, N. Fernández, D. Jaque and E. Ximendes, *ACS Nano*, 2020, **14**, 4122–4133.
31 L. Yao, Y. Li, D. Xu, H. Lin, Y. Peng, S. Yang and Y. Zhang, *New J. Chem.*, 2019, **43**, 3848–3855.
32 N. Katumo, G. Gao, F. Laufer, B. S. Richards and I. A. Howard, *Adv. Opt. Mater.*, 2020, **8**, 2000507.
33 K. Trejgis, M. D. Dramićanin and L. Marciniak, *J. Alloys Compd.*, 2021, **875**, 159973.
34 M. G. Brik, S. J. Camardello and A. M. Srivastava, *ECS J. Solid State Sci. Technol.*, 2014, **4**, R39–R43.
35 L. M. W. Piotrowski, M. Kuchowicz and M. Dramićanin, *Chem. Eng. J.*, 2021, 131165.
36 M. P. Pechini, *US Pat.*, 3330697, 1967, p. 2.
37 L. F. Mattheiss, *Phys. Rev. B: Solid State*, 1972, **6**, 4740–4753.
38 T. S. Chang, *J. Appl. Phys.*, 1972, **43**, 3591–3595.
39 C. P. Enz, *Phys. Rev. B: Solid State*, 1972, **6**, 4695–4702.
40 M. Cardona, *Phys. Rev.*, 1965, **140**, A651–A655.
41 R. Pazik, M. Maczka, M. Malecka, L. Marciniak, A. Ekner-Grzyb, L. Mrowczynska and R. J. Wiglusz, *Dalton Trans.*, 2015, **44**, 10267–10280.
42 C. Matuszewska, K. Elzbieciak-Piecka and L. Marciniak, *J. Phys. Chem. C*, 2019, **123**, 18646–18653.
43 R. D. Shannon, *Acta Crystallogr., Sect. A: Cryst. Phys., Diffr., Theor. Gen. Crystallogr.*, 1976, **32**, 751–767.
44 Z. Bryknar, V. Trepakov, Z. Potůček and L. Jastrabík, *J. Lumin.*, 2000, **87-89**, 605–607.
45 M. G. Brik, *J. Phys. Chem. Solids*, 2006, **67**, 856–861.
46 H. Kato, Y. Takeda, M. Kobayashi, H. Kobayashi and M. Kakihana, *Front. Chem.*, 2018, **6**, 467.
47 A. Tkach, P. M. Vilarinho and A. L. Kholkin, *Acta Mater.*, 2005, **53**, 5061–5069.
48 H. Yang, K. Kan, J. Ouyang and Y. Li, *J. Alloys Compd.*, 2009, **485**, 351–355.
49 V. Trepakov, M. Makarova, O. Stupakov, E. A. Tereshina, J. Drahokoupil, M. Čerňanský, Z. Potůček, F. Borodavka, V. Valvoda, A. Lynnyk, A. Jäger, L. Jastrabik and A. Dejneka, *Mater. Chem. Phys.*, 2014, **143**, 570–577.
50 M. G. Brik and N. M. Avram, *J. Phys.: Condens. Matter*, 2009, **21**, 155502.

